Tuneable Permeability to H_2, CO_2, He, and Ar in Graphene Oxide–PDDA Self-Assembled Multilayers, Yielding Good Selectivity at High Flux

Giacomo Foli, Alessandro Kovtun, Fabiola Liscio, Elena Battaglini, Simone Ligi, Maurizio Fiorini, Matteo Minelli,* and Vincenzo Palermo*

Today, the most effective and suitable method to obtain molecular H_2 is the extraction from mixtures where it is present, using gas-sieving membranes. To this aim, the preparation and characterization of layered nano-composites are described, made of alternated layers of positively charged Poly(Diallyl Dimethyl Ammonium chloride) (PDDA) and negatively charged graphene oxide (GO) nanosheets with high and tunable selectivity for H_2 purification. The composites are assembled exploiting electrostatic interactions and the layer-by-layer technique; this study correlates permeance tests with changes in chemical composition and structure of the material using X-rays Photoelectron Spectroscopy, X-rays diffraction water contact angle, and surface zeta-potential measurements. Thanks to its layered nature, the GO-PDDA composite shows an excellent selectivity, allowing faster permeation of H_2 as compared to CO_2 and Argon. By transforming the GO to reduced GO, the porosity of the nanosheets can be further increased, in this way increasing the permeance of the material and its selectivity at the same time, thus allowing to overcome the Robeson limit, the technological upper boundary to the performance of actual membranes.

1. Introduction

Climate change is a clear and present danger which spurs governments of the world to intervene with concrete solutions.[1,2] The reckless exploitation of resources combined with anthropogenic atmospheric emissions are seriously altering delicate equilibria that allow our life on this planet.[3] It is well-known that the emission of green-house gases is provoking the global warming observed in the last decades.[4] Carbon dioxide (CO_2), generated by combustion of fossil fuels, is probably the most conspicuous green-house gas[5] and, for this reason, an energetic transition towards a hydrogen-based and carbon neutral economy was recently spurred by European Commission.[6]

Despite its abundance in the universe,[7] elemental hydrogen, existing as bimolecular H_2, is not present on our planet. Due to its low density, a hydrogen molecule would rapidly reach highest layers of our atmosphere and escape from it.[8] The electrolysis of water allows to prepare pure H_2, but is expensive.[9] Thus, the most effective and suitable method to obtain and stock molecular H_2 is the extraction from mixtures where it is present, following proper reaction procedures.[10] Reforming of fossil feedstocks is a mature technology that allows the production of bimolecular hydrogen, but it causes concomitant production of CO_2.[11] Thus, the productive potential of this technology rests on the identification of suitable strategies to separate H_2/CO_2 gas mixtures.[12] Amine scrubbing can be employed to this aim, due to the acid character of carbon dioxide, and it is widely recognized as the state-of-the-art technology to sequestrate CO_2 from a generic gas mixture.[13] Unfortunately, the high cost of operation associated with scrubbing plants[14] does not permit to purify H_2

G. Foli, A. Kovtun, V. Palermo
Institute for Organic Synthesis and Photoactivity (ISOF) – National Research Council of Italy (CNR)
via Piero Gobetti 101, Bologna 40129, Italy
E-mail: vincenzo.palermo@isof.cnr.it

F. Liscio
Institute for Microelectronics and Microsystems (IMM) – National Research Council of Italy (CNR)
via Piero Gobetti 101, Bologna 40129, Italy

E. Battaglini, M. Fiorini, M. Minelli
Department of Civil, Chemical, Environmental, and Materials Engineering (DICAM)
Alma Mater Studiorum - University of Bologna
via Umberto Terracini 28, Bologna 40131, Italy
E-mail: matteo.minelli@unibo.it

S. Ligi
Graphene-XT S.r.l.
Via d'Azeglio 15, Bologna 40123, Italy

at an energy-vector price. While a conventional cryogenic distillation could be employed, membrane separation could be a valuable alternative.[15] The low demand of energy required and the simple scale-up of such separation technique prompted intensive research in this field, to identify new and more attractive purification strategies. In particular, polymer-based membranes are able to guarantee interesting separation performances, as well as robustness and durability, required by the application. H_2 and CO_2 molecules have different condensability, kinetic diameter, or chemical reactivity,[16] and thus could be separated using a suitable membrane.[17] According to the solution-diffusion concept, the mechanisms of molecular transport in dense layers occurs in two steps.[18] First, approaching gas molecules interact with membrane surface and solubilize. Second, molecules diffuse through the membrane and, drove by a pressure gradient, reappear on the other side.

The steady-state gas flux (J) through a membrane depends on both membrane thickness (l) and pressure difference (Δp) according to the following equation:

$$J = P \cdot \frac{\Delta p}{l} \tag{1}$$

where the proportional coefficient (P) is the permeability coefficient, conventionally expressed in barrer, a non-SI unit (1 barrer $= 3.35 \times 10^{-16}$ mol m^{-1} s^{-1} Pa^{-1}). The incorporation of the thickness of the membrane into a more application-oriented quantity, permeance (Q), leads to:

$$Q = \frac{P}{l} = \frac{J}{\Delta p} \tag{2}$$

Given that typical membranes are characterized by submicrometric thickness in order to achieve the largest transmembrane fluxes with a given material (i.e., at fixed permeability),[19] permeance Q is usually expressed in GPU (gas permeation units), corresponding to barrer μm^{-1}.

The transport of gas molecules through a membrane could be modelled using two coefficients related to solubility (S) and diffusion (D), according to the solution-diffusion concept previously mentioned:

Permeability P and permeance Q differ for different gases permeating in a given material, thus allowing their separation in the membrane layer. The preferential transport of one gas with respect to another is quantified by the ratio of the pure gas permeabilities or permeances (i.e., selectivity):

$$\alpha_{H_2/CO_2} = \frac{P(H_2)}{P(CO_2)} = \frac{Q(H_2)}{Q(CO_2)} \tag{3}$$

A membrane suitable for industrial applications should combine high separation efficiency and high flow rate, i.e., have both P and α very high.[20] Unfortunately, in dense polymeric membranes, when selectivity increases, permeation decreases, thus yielding an empirical limit related to membrane process, the so-called Robeson's upper bound.[21] Robeson's limit for the purification of H_2 could be circumvented by employment of palladium-based membranes,[22] characterized by a (theoretical) infinite selectivity towards hydrogen transport, thus ideal for H_2/CO_2

separation.[23] Unfortunately, high prices of metallic raw materials combined with the difficult membrane fabrication and maintenance prevented the utilization of metallic membranes in commercial applications.[24] On the other hand, dense membranes made of polymeric materials are undoubtedly cheaper, and can be effectively employed in gas separation processes.[25]

The gas sieving efficiency of some polymers could be further improved by fabrication of proper composites.[26] Among various possibilities, 2D nanosized materials such as Graphene Oxide (GO) revealed a great potential in gas separation applications.[27] Due to its peculiar shape, a single GO sheet resembles an angstrom-thick membrane and has the potential to affect transport of gases acting as an obstacle to diffusing molecules.[28] GO-based composite membranes, prepared by means of several techniques such as vacuum-assisted deposition or spray-evaporation,[29,30] were used with success to purify H_2 from CO_2, even if with low selectivity.[31–33] The surface of GO nanosheets is densely populated by hydroxyl, carboxy, and epoxy groups groups,[34] which make GO easily processable, even in water, and the fabrication of GO membranes cheap and scalable.[35] Such oxygen containing groups are often considered as defects to remove, mainly to restore the electrical conductivity of the material.
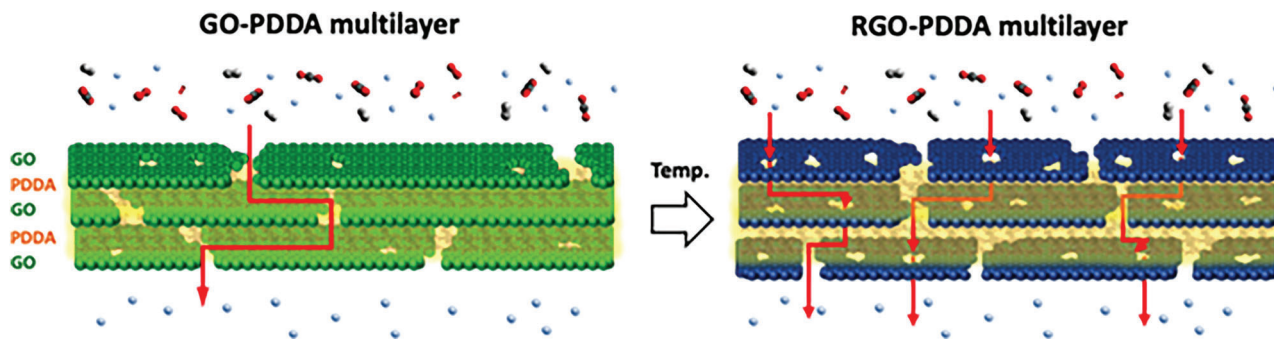
The presence of polar or charged chemical groups on the surface of GO nanosheets can be exploited to create novel supramolecular architecture, using electrostatic interactions to promote the self-assembling of layered, hierarchical composites.[36–38]

We previously demonstrated the production of laminates based on alternate stacked layers of GO and polymers[39] prepared by layer-by-layer (LbL) self-assembly,[40] with excellent gas sieving performance. Such method makes use of the partial negative charge of GO due to functional groups, which can interact electrostatically with a suitable positively charged polyelectrolyte, i.e., a polycation.

The electrostatic repulsion between similar molecules limits the amount of material deposited at each step, while the electrostatic attraction between GO and the polymer yields consistent, uniform coatings on macroscopic scale, as described in detail in a previously published work.[39]

GO nanosheets have a lateral size of tens of microns and a thickness <1 nm,[41] featuring thus a large aspect ratio, much larger than what obtainable in exfoliated graphene nanosheets, leading thus to superior performances in terms of gas selectivity but also low values of permeance. Other works in literature showed the possibility to generate nano-sized holes on the GO surface to overcome this obstacle.[42] As example, Zhao and co-workers developed a plasma-based etching strategy suitable to generate angstrom-sized pores on single-layer graphene, achieving superior gas separation factors.[43] Similarly, improved perm-selectivity performances were achieved by incorporating in a polymer matrix a chemically porous reduced graphene oxide (RGO).[44] Indeed, the removal of oxygen-containing functional groups from the GO nanosheets generates defects on the graphenic layers eventually leading to an increase of gas permeability and selectivity. Interestingly, porous RGO could be prepared also by simple thermal treatments.[45]

In this work, we combine our LbL approach with the ones typically used to create nanopores on graphene and GO. To this aim, we fabricated GO laminates by means of a

**ADVANCED
SCIENCE NEWS**
www.advancedsciencenews.com

**ADVANCED
MATERIALS
INTERFACES**
Open Access
www.advmatinterfaces.de

Scheme 1. GO and PDDA multilayers are created using a layer-by-layer technique based on electrostatic interactions. Then, porosity and permeability to gases is tuned by transforming the GO in RGO, without affecting significantly the PDDA polymer.

dip-coating layer-by-layer technique, alternating the deposition of graphenic nanosheets with a positively charged polyelectrolyte, Poly(diallyldimethylammonium Chloride), PDDA, industrially used as a flocculant due to its high charge density.[46] In detail, a ten Bi-Layers architecture, named $(PDDA/GO)_{10}$, was self-assembled on a commercial polyimide support, Matrimid5218. We measured permeance values Q of differently sized penetrant gases for the multilayers, and explored the possibility to tune the permeability of the GO nanosheets by a simple post-fabrication in-vacuum thermal treatment (annealing) to transform the GO nanosheets present in the composite into porous RGO nanosheets (**Scheme 1**).

2. Results and Discussion

We produced our material using a procedure based on successive and alternated deposition of few nanometers thick layers of oppositely charged species. Each sample was dipped multiple times first in a solution of positively charged PDDA (1 wt%), then in a suspension of negatively charged GO (0.015 wt%). The procedure was repeated ten times to obtain a layered structure of 10 PDDA-GO bilayers (BLs). The first dipping stage was always in PDDA, due to the good interaction of positively charged PDDA with the superficially hydrolyzed Matrimid. This layered structure is termed $(PDDA/GO)_{10}$ hereafter.

To confirm that electrostatic interaction is indeed the mechanism driving the self-assembly process, we monitored at each step the superficial ζ-potential of the growing multilayer (**Figure 1**a; Table S1, Supporting Information). We observed a switch of the surface potential from $\approx+20$ mV (after PDDA deposition) to ≈-40 mV (after GO deposition). The latter term agrees well with the ζ-potential of GO measured in solution.[47–49]

The potential variation was more irregular for the first two bilayers, likely due to incomplete coating on the Matrimid substrate. Deposition of additional bilayers provided a consistent and regular oscillation of the potential. The binary nature of our layered material was also confirmed by Water Contact Angle measurements (WCA), which showed an analogous oscillation. Namely, WCA was $62° \pm 2°$ after GO deposition, and $45° \pm 3°$ after PDDA deposition (insets in Figure 1c,d; Table S2, Supporting Information); the higher hydrophobicity of GO can be attributed to the presence of non-charged sp^2 domains in the carbon network. SEM analysis showed the typical wrinkles of graphenic sheets clearly visible on the GO terminated structure,

$(PDDA/GO)_{10}$ Figure 1c, partially coated when PDDA was the outmost layer $(PDDA/GO)_{9.5}$ Figure 1d.

The chemical composition of the membrane active layer was confirmed by XPS analysis (Figure 1b and **Table 1**; Table S3, Supporting Information) carried out on ad hoc Matrimid coated Si wafers (see Experimental Section). To obtain an accurate, quantitative evaluation of the chemical species present in the material, in particular of the aromatic C sp^2, we fitted the XPS C 1s signal using an asymmetric pseudo-Voigt line-shapes (APV) to model the aromatic C sp^2 component. Such approach is similar to what used for metallic components that are fitted using asymmetric line-shapes. This is in contrast to symmetric, Gaussian-based line-shape approaches conventionally used in fitting XPS spectra. The use of APV fitting allows better accuracy in quantifying C 1s contributions, as we previously demonstrated by systematic XPS studies[50] on graphene-based materials in order to obtain a reliable composition of C—C and C—O groups from C 1s fit and – as a direct consequence – achieve a good estimation of the O/C atomic ratio independently from the O 1s signal, that may rise from oxygen-rich substrates (i.e., native silicon oxide). The common symmetric pseudo-Voigt line-shape for all the other components of the XPS signal.

The efficient shielding of any XPS signal from the Silicon substrate was used as an indicator of effective, uniform coating. Thanks to the efficiency of the electrostatic-driven LbL coating of PDDA and GO, the Si signal became extremely low (<0.6%) as measured by XPS on a large area, ≈20 mm^2. The main signals observed were C 1s, O 1s, N 1s from both GO and PDDA, with minor peaks (<0.6%) attributed to Na 1s, S 2p, and Si 2p. Noteworthy, the peak attributed to Chlorine ions, clearly visible in the spectrum recorded upon PDDA$^+$Cl$^-$ deposition, completely disappeared in $(PDDA/GO)_{10}$. The absence of Cl 2p signal supported the proposed self-assembly mechanism, where a complete "ion-exchange" took place between Cl$^-$ counter-ion and the negatively charged GO. Both GO and PDDA were mainly composed by carbon and oxygen; furthermore, the C 1s signal of $(PDDA/GO)_{10}$ and that of GO are similar (Figures S4b and S5, Supporting Information), thus the quantitative analysis of the multilayer was a non-trivial issue. The presence of a strong signal due to C—O and C=O groups in $(PDDA/GO)_{10}$ suggested that the film was mainly composed by GO (Figure S5, Supporting Information). The N signal at 402.3 eV and 1.1% relative atomic abundance found in the as prepared $(PDDA/GO)_{10}$ was instead univocally associated to PDDA.[51] The N signal in the composite
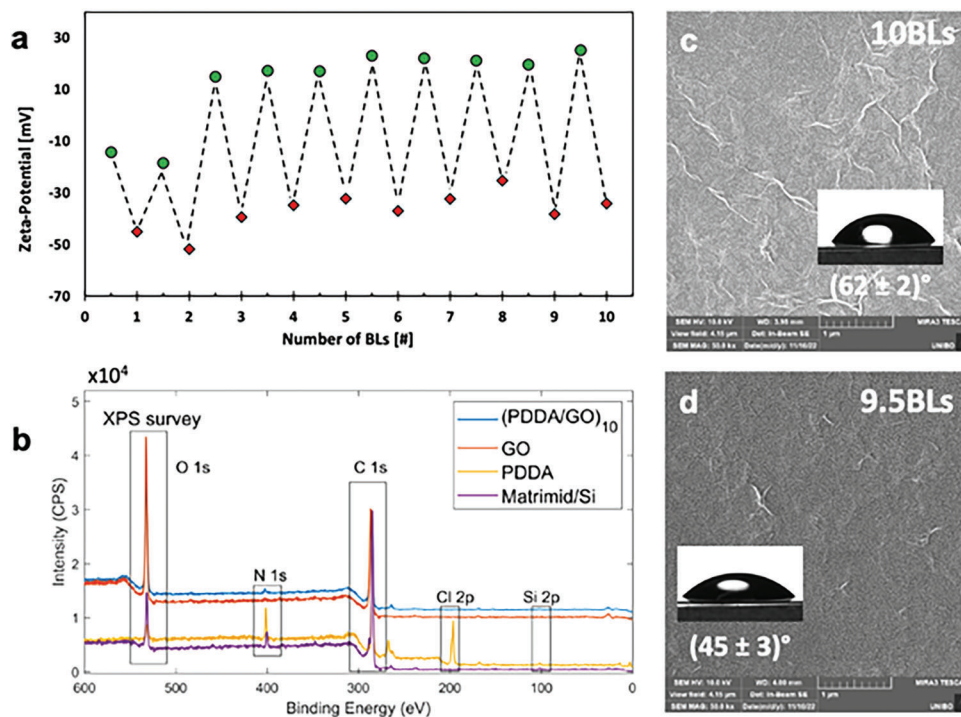
Figure 1. a) Surface ζ-potential measured on the external layer of the growing PDDA-GO multilayer membrane: green circles indicate PDDA terminated samples, red squares GO-terminated ones, each experimental point is the average of at least three measurements on three independent samples. b) XPS spectra of self-assembled multilayer, and building-blocks used. c) SEM imaging of the GO-terminated surface of the multilayer, i.e., 10BLs. d) SEM imaging of the PDDA-terminated surface of the multilayer, 9.5 BLs. The insets of (c,d) show the respective water contact angles (WCA) and the average WCA (obtained from measurement on three different specimens).

was slightly shifted respect to the N 1s at 401.8 eV of pure PDDA (Figure S3, Supporting Information). Such slight chemical shift for N 1s atoms of PDDA could be attributed to the change of Cl⁻ counter-ion with GO.

The relative amount of PDDA in $(PDDA/GO)_{10}$ could be estimated by XPS data and stoichiometric considerations. The pristine PDDA had a stoichiometric ratio C:N:Cl of 8:0.8:1, very similar to the theoretical one (8:1:1), corresponding to a nitrogen content $N = 7.4\%$. Nitrogen in $(PDDA/GO)_{10}$ was instead $N = 1.1\%$, indicating that most of the composite was made of GO (Figure S1b, Supporting Information). We could estimate the PDDA loading x in the composite with a simple averaging formula:

$$N_{composite} = x\, N_{PDDA} + (1 - x)\, N_{GO} \tag{4}$$

where N is the atomic fraction of nitrogen atoms measured in the composite, in pure PDDA, and in pure GO (1.1%, 7.4%, and 0.3%, respectively). We obtained a PDDA loading in the compos-
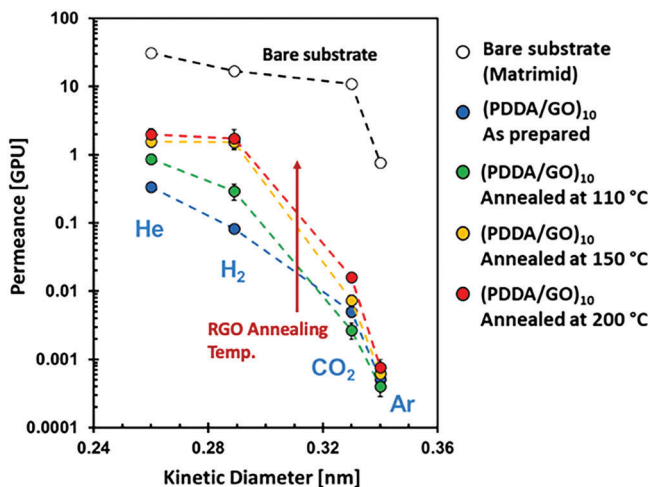
ite $x \approx 11\%$, based on atomic abundance. It was not possible to translate this atomic loading in weight loading because XPS cannot estimate hydrogen atoms or water molecules contained in GO and PDDA, which also contribute to the total weight.

However, we could estimate the coverage of PDDA on the GO nanosheets, in molecules per nm^2. For this, we combined the measurements of N and C peaks with the known stoichiometry of PDDA.

We calculated that in the composite, for every 100 atoms we have 63.4% C atoms of GO and 1.1% N atoms (carbon atoms belonging to PDDA were removed from this calculation). The ratio between these two quantities correspond to ca. one PDDA monomer every 58 atoms of carbon; this ratio could be translated in one PDDA molecule every $\approx 1.5\ nm^2$ of GO nanosheet. This estimate is indicative not including carbons removed due to pore defects always present in GO; it seems though reasonable, giving that the lateral size of a PDDA monomer is ≈ 0.5 nm, and suggests that the coverage of disordered PDDA chains on GO is only partial, leaving space for diffusion of gas molecules.

Table 1. Elemental composition of pure PDDA, pure GO, and the self-assembled multilayer, determined by XPS analysis.

Sample	C 1s [at%]	O 1s [at%]	N 1s [at%]	Si 2p [at%]	Cl 2p [at%]	S 2p [at%]
PDDA	78.0 ±0.9	3.4 ±0.3	7.4 ±0.3	0.9 ±0.1	9.3 ±0.3	0.7 ±0.1
GO	72.2 ±0.9	27.1 ±0.5	<0.2	–	–	0.4 ±0.1
$(PDDA/GO)_{10}$	72.2 ±0.9	25.4 ±0.5	1.1 ±0.1	0.5 ±0.1	–	0.4 ±0.1

**ADVANCED
SCIENCE NEWS**

www.advancedsciencenews.com

**ADVANCED
MATERIALS
INTERFACES**
Open Access

www.advmatinterfaces.de

Figure 2. Permeance of the tested gas molecules in (PDDA/GO)$_{10}$ multilayers as prepared (blue circles) and annealed at the various temperature: 110 °C (green circles), 150 °C (orange circles), and 200 °C (red circles). For the sake of comparison, permeance of the bare substrate (Matrimid) is also included (empty circles), calculated with a 1 µm reference thickness. Each experimental point is the average of at least three measurements on three independent samples.

The permeability of the pristine, as prepared, (PDDA/GO)$_{10}$ multilayer was then tested for different gases characterized by different molecular size, listed in order of increasing kinetic radius r: He (0.26 nm), H$_2$ (0.29 nm), CO$_2$ (0.33 nm), and Ar (0.34 nm). In particular, selective permeability of H$_2$ and CO$_2$ is of great interest for hydrogen purification. The blue line in **Figure 2**a shows the permeance (expressed in GPU) of the (PDDA/GO)$_{10}$ composite to the four different gases. Noteworthy, the pristine PDDA/GO coating acts as an effective barrier against all gases as compared to the bare Matrimid substrate (calculated with a 1 µm reference thickness), decreasing permeance of 2–4 orders of magnitude, thus confirming the absence of macroscopic cracks or leaks on the whole surface of all the samples tested. The semi-logarithmic plot shows that permeability is (roughly) exponentially dependent on kinetic radius, in agreement with previous results,[39] indicating that the contribution of diffusivity to the permeation process is predominant. Three measurements taken on three independent samples are shown for each gas, confirming again the good uniformity of the LbL coating procedure and of the permeability tests.

The PDDA/GO samples were then treated for 1 h at different temperatures (100, 150, and 200 °C) under vacuum. It is well known that both chemical and physical properties of GO can be tuned by chemical, thermal, or electrochemical treatments, transforming it in reduced graphene oxide (RGO). Such treatment is typically performed to increase the electrical conductivity of the material given that GO is insulating while RGO conductivity is better than the one of most conducting polymers.[52] Here, though, we were interested in the structural changes ongoing during the reduction, rather than the electrical ones. The thermal treatment transforming GO to RGO may remove the oxygen-containing moieties present in GO in the form of polar hydroxy, carboxy, or epoxy groups, restoring part of the sp^2 domains typical of pristine graphene.[53] The final structure, though, is not

graphene but RGO, characterized by structural defects in the form of pores and voids in the graphene structure, usually under 5 nm^2 in size,[54] which can accommodate small molecules or atoms, as shown by experimental and computational studies.[55] Thus, RGO is chemically more similar than GO to graphene, but also features a more porous structure than GO. The formation of such pores is expected to positively affect the permeance of the multilayer for gas molecules.
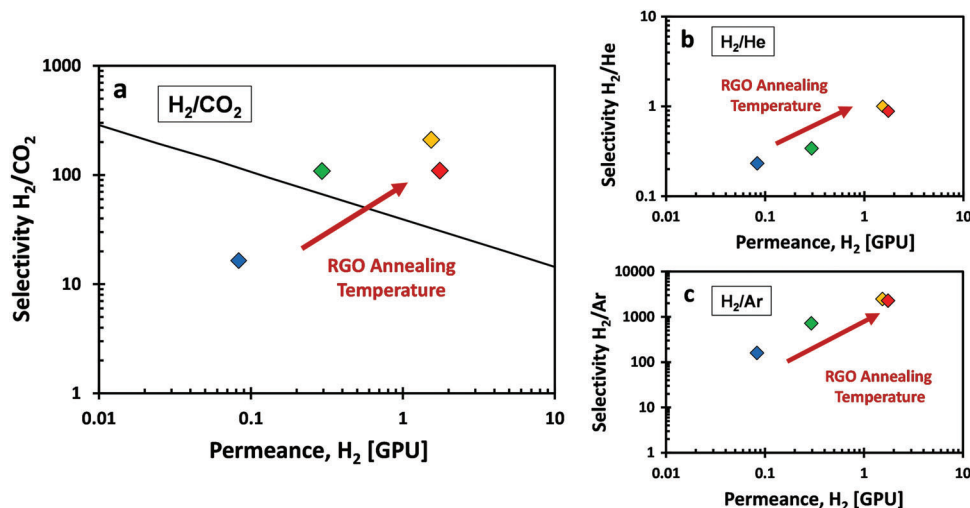
The gas transport properties in such structure was strongly affected by such treatment, as one can see in Figure 1b. An increase of permeance of all gases could be observed at higher annealing temperatures; however, the increase was not uniform for all gases, being negligible for larger Ar atoms, and significant for smaller He and H$_2$ molecules (Figure 2). This agrees well to what observed in previous results, where the different permeance of small molecules in layered materials was ascribed to differences in molecular dimension.[39] No clear correlation was found, instead, with critical volume of the tested gas (Figure S2, Supporting Information).

The different increase in permeance also enhanced significantly the selectivity of (PDDA/GO)$_{10}$ multilayers for gas separation. **Figure 3**a reports the Robeson Plot for the targeted separation, with H$_2$/CO$_2$ selectivity plotted versus total H$_2$ permeance. The Robeson plot of H$_2$ with respect to differently sized penetrants, He and Ar, is also reported for comparison in Figure 3b,c. The ideal material would sit on the top right corner of each graph, i.e., have high selectivity combined with high H$_2$ flux, overcoming the actual technological limits.[21] We can see that in all cases, selectivity increases going from pristine samples to samples annealed at 110 °C and even more at 150 °C. In case of H$_2$/He, (Figure 3b) such improvement is small, with selectivity being ≈1 in all cases (i.e., no selective permeance for hydrogen respect to helium). Conversely, the selectivity of H$_2$/CO$_2$ (Figure 3a) increases from 16 to 108 upon annealing at 110 °C, and to 209 after annealing at 150 °C. Also, selectivity for H$_2$/Ar goes from 161 to 721, then to 2480, Figure 3c. A full list of the permeance data is reported in Table S2 (Supporting Information).

For all couples, further annealing at 200 °C did not provide additional benefit; H$_2$ permeance increased slightly, but a small decrease of selectivity was also observed.

By comparing Figure 2 with Figure 3, we can see that the large improvement in H$_2$ selectivity is due to a significant increase of the H$_2$ permeance, rather than to a decrease of permeance of the other gases (see also original data in Table S3, Supporting Information). The permeance of H$_2$ in annealed (PDDA/RGO)$_{10}$ composites increased from 0.083 GPU to 1.75 GPU upon annealing. Indeed, the annealing performed at 110 °C was already sufficient to overcome the actual Robeson upper bound for the separation of H$_2$/CO$_2$ mixture.

Such behavior is attributed to the thermal treatment effect on the graphene oxide. In order to confirm such hypothesis, any significant effect of the thermal treatment on the PDDA layer contained in (PDDA/GO)$_{10}$ should be ruled out. A certain extent of polymer modification was observed in neat PDDA thin films by XPS upon annealing (Figure S9, Supporting Information). However, we self-assembled for comparison a multilayered material replacing the GO nanosheets with a polymeric anion, Poly(sodium-4-styrene sulfonate), PSS. We used the same multi-deposition procedure described above to

**ADVANCED
SCIENCE NEWS**

www.advancedsciencenews.com

**ADVANCED
MATERIALS
INTERFACES**

www.advmatinterfaces.de

Figure 3. Selectivity of H_2 with respect to a) Carbon dioxide, b) Helium, and c) Argon, plotted versus absolute H_2 permeance of $(PDDA/GO)_{10}$ multilayers. Symbols indicates samples as prepared (blue diamonds) and annealed at the various temperature: 110 °C (green diamonds), 150 °C (orange diamonds), and 200 °C (red diamonds). The black line in (a) indicates the current Robeson upper bound.

self-assemble $(PDDA/PSS)_{10}$. XPS confirmed that in this material PDDA and PSS were close to ideal 1:1 ratio (N/S ratio from N 1s signal and S 2p signal was 0.9, see Figure S10a, Supporting Information). We then treated and characterized such polymer–polymer multilayers as done for the PDDA/GO multilayers. Permeance of $(PDDA/PSS)_{10}$ before and after annealing at 200 °C did not change appreciably; furthermore, this composite failed to provide any gas barrier, yielding a performance that was comparable to the one of bare Matrimid (Figure S10c, Supporting Information). Thermogravimetric analysis of the PDDA revealed a slight degradation of the polycation in the annealing temperature range (110–200 °C, Figure S10b, Supporting Information) confirming the degradation observed from XPS spectra. A slight degradation was observed in PSS as well, Figure S10b (Supporting Information).

The main effect of the thermal treatment on permeance can thus be attributed to the GO layer, as revealed by the analysis of the chemical evolution of the $(PDDA/GO)_{10}$ multilayers using XPS. We used a previously discussed fit procedure to quantify with high accuracy C 1s contributions from graphitic carbon (sp^2), defects (sp^3 carbon), carbons bonded to hydroxyl and epoxy groups, and from carbonyl and carboxyl groups.[50] Regrettably, the presence of C−N groups in PDDA gave a signal superimposed to C−O groups in GO, making ambiguous the distinction between these two groups; thus, we could use only the peak associated with the graphitic carbon (sp^2) at energy 284.4 eV as reliable structural information of PDDA/GO annealed at different temperatures.

Figure 4a showed that a decrease in O/C ratio took effectively place during the annealing, as expected in GO reduction. As
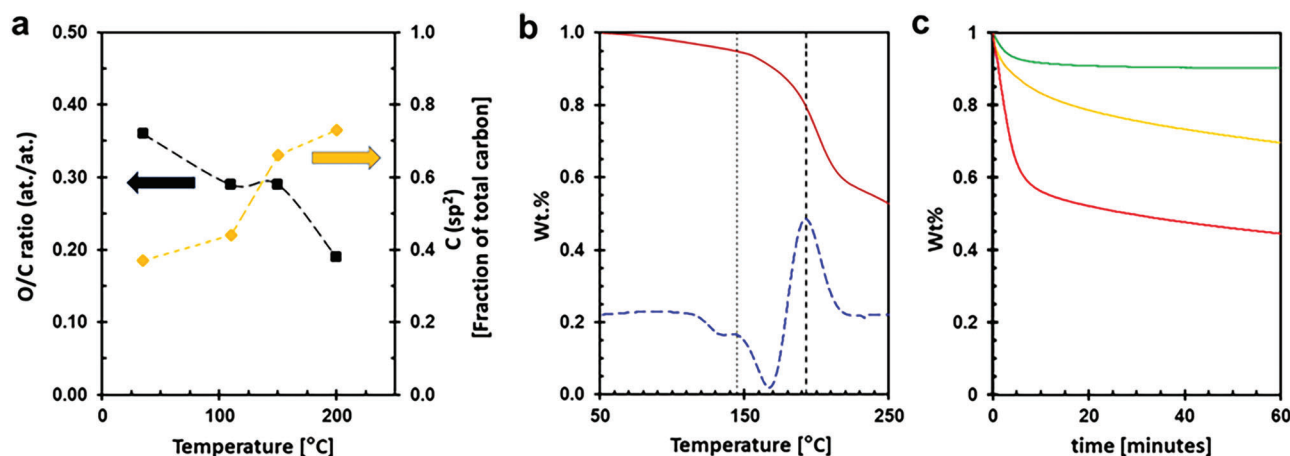
Figure 4. a) Evolution of O/C ratio in the multilayer with the increase of the temperature of annealing and variation of sp^2 chemical groups present in the multilayer as determined by XPS. b) Thermogravimetric of GO. c) Isothermo-gravimetric analysis of GO at different T: 110 °C (green curve), 150 °C (orange curve) and 200 °C (red curve). Curves reported in (d) are the average of three independent experiments conducted at the various temperature of annealing (see also Figure S12b, Supporting Information).
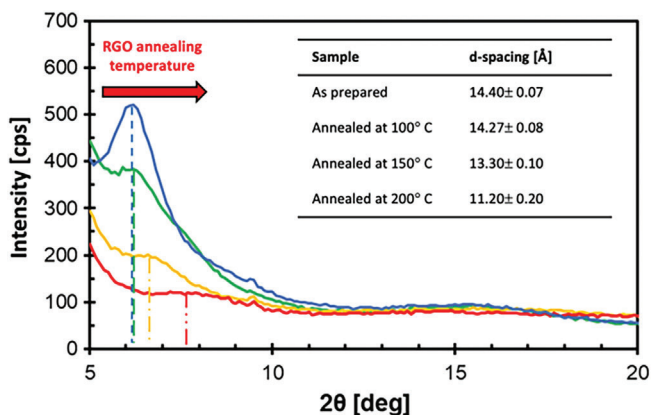
**ADVANCED
SCIENCE NEWS**

www.advancedsciencenews.com

**ADVANCED
MATERIALS
INTERFACES**
Open Access

www.advmatinterfaces.de

Figure 5. XRD patterns recorded for the as prepared and annealed multi-layers.

predictable from previous experiments, no variation in O/C ratio was observed after the 200 °C annealing of the polymer–polymer multilayer, see Table S4 (Supporting Information) entry $(PDDA/PSS)_{10}$ and $(PDDA/PSS)_{10}@200C$. Figure S6 (Supporting Information) shows the evolution of the chemical structure of $(PDDA/GO)_{10}$ as a function of annealing temperature, as measured by XPS; the deoxygenation and partial graphitization were evident from the decrease O/C ratio and the increase of C=C sp^2, in the C 1s signal, both features being typical of thermal reduction of GO. Thermogravimetric analysis (TGA, Figure 4b) performed on neat GO revealed that graphenic sheets underwent a first decomposition at roughly 145 °C. A second and more pronounced evolution of gases took place at 192–195 °C. Such observations are in agreement with the isothermo-gravimetric curves recorded for neat GO at the temperatures used for the diverse annealing: 110, 150, and 200 °C (Figure 4c). Indeed, while a negligible loss of weight was observed after 1 h at 110 °C, a significant decrease was observed at 150 °C, a temperature slightly higher than the first degradation temperature observed by TGA. Finally, a large and vigorous degradation was observed after 1 h at 200 °C, in agreement with what observed in the TGA curve. For comparison, we performed the same isothermal analysis on neat PDDA. In that case, the loss of mass recorded after 1 h of isotherm was negligible (Figure S11, Supporting Information). This also confirms that the changes in permeance observed for annealed $(PDDA/GO)_{10}$ cannot be due to degradation of PDDA, but should be caused by changes in the GO.

The thermal treatment and the resulting (partial) reduction of GO nanosheets are expected to alter the multilayer structure. We used X-ray diffraction (XRD) to characterize the membrane's bi-layer periodic spacing (d-spacing) to inspect any correlation with the gas permeation results. XRD patterns in **Figure 5** shows a peak shift towards higher angles, consistent with the decrease in interlayer d-spacing induced by the annealing. d-spacing in pristine $(PDDA/GO)_{10}$ is 14.4 Å. It decreases to 14.27, 13.3, and 11.2 Å upon annealing to 110, 150, and 200 °C respectively. This shrinking is commonly observed in GO stacks and can be attributed to the removal of bulky oxygen-containing groups which act as spacers between the GO layers. Indeed, the magnitude of d-spacing contraction at 200 °C (≈-3 Å) is compatible with what was observed in pristine GO film,[56] where d-spacing roughly de-creases from 10–8 Å down to 5 Å. The peak broadening with thermal annealing is related to the loss of packing order inside the multilayer. [57,58]

The structural variation cannot explain the permeance improvement (Figure 2), because experimental evidence from the literature indicates that d-spacing should be increased with tailored spacers to increase diffusion and permeability.[57,58]

Therefore, the increase in gas permeability of the annealed coating has to be ascribed to one of the peculiar effects of RGO reduction, with an increase in porosity due to carbon being removed during the reduction. Indeed, as revealed by FT-IR spectra of chemical species evolved during the iso-thermo-gravimetric analysis at the different temperatures of annealing, CO_2 release was detected at all temperature (double peak at roughly 2300 cm^{-1}, Figure S15, Supporting Information). Moreover, presence of CO was observed performing the annealing at 200 °C (double peak at roughly 2100 cm^{-1}, Figure S15, Supporting Information). Interestingly, in all cases evolution of gaseous species was negligible after 500 s of annealing. Such an observation suggested that the investigated thermal reduction of GO mainly took place in the first instant of annealing, probably due to a sort of thermic shock. The removal of carbon atoms is known to create pores of nanometric size in the RGO sheets[54] and the presence of such pores could explain the enhanced permeance observed for all gases. The presence of such distributed nano-pores was sufficient to increase permeance values but, noteworthy, did not degrade the selectivity imparted by the layered structure. Moreover, such a layered structure undergoes a sort of crinkle, testified by the loss of sharpness of the XRD peak ascribed to GO layers, and consequently generating an additional porosity. Indeed, as shown in Figure 3, after annealing the permeance for the smallest tested penetrants, i.e., He and H_2, increased significantly, in particular for H_2. On the other hand, the permeance of larger probes such as CO_2 and Ar showed only minor increase, indicating an effective and average pore size to be located in between H_2 and CO_2 molecular dimensions. The final result was to improve overall selectivity, as observed for all gas couples in Figure 3.

3. Conclusion

We described the preparation of an electrostatically controlled supramolecular architecture named $(PDDA/GO)_{10}$ using electrostatic interactions and a layer-by-layer self-assembly procedure. We followed the alternated deposition of polycationic chains (PDDA) and sheets of GO, monitoring the superficial ζ-potential of the outmost layer of the growing structure. The XPS spectrum of the fabricated laminate highlighted how an effective ion-exchange took place during deposition of the oppositely charged species. Given the potential application of such aggregate as a gas sieving system, we decided to test perm-selectivity performances for He, H_2, CO_2, and Ar gases. After testing the permeance of the pristine $(PDDA/GO)_{10}$, we annealed the samples in vacuum at three different temperatures: 110, 150, and 200 °C, in an attempt to increase the permeance of the multilayer by generating pores produced during the conversion of GO present in the multilayer into RGO. An increase of performance for the gas couple H_2/CO_2 was observed in all annealed multilayers, outperforming currently available sieving system, with the best perm-selectivity reached at $T = 150$ °C. XRD analysis confirmed that a

2300357 (7 of 10)

**ADVANCED
SCIENCE NEWS**

www.advancedsciencenews.com

**ADVANCED
MATERIALS
INTERFACES**
Open Access

www.advmatinterfaces.de

rearrangement of coating architecture was achieved after the annealing, and a more spaced and disordered multilayer was obtained increasing the temperature of annealing. At the same time, XPS spectra confirmed reduction of GO by increasing temperature used during the annealing. Comparison experiments excluded a possible effect of PDDA on the improvement of performances in perm-selectivity observed for the annealed multilayers, allowing to attribute the observed changes mainly to changes in the deposited GO nanosheets.

Thanks to the combination of materials and to their stacked arrangement and post-processing, we could achieve very high selectivity, up to 108 for H_2/CO_2 (Figure 3a) and up to 2480 for H_2/Ar, Figure 3c. This is significantly higher than what obtained, as example, for GO or graphene multilayers on PMMA, which achieved H_2/CO_2 selectivity = 40 for samples annealed at 140 °C.[28]

Noteworthy, the local rearrangement of packing observed upon annealing resembles previous results observed in GO-polyamine composites by Andreeva et al.[59] In those materials, obtained by simple mixture in solution of GO and polymer, the rearrangement was due to a chemical trigger, namely change in pH, which created changes in the inter-sheet spacing and hopping paths for ion permeation. In our case, the loss of packing is instead triggered by temperature, and will enhance diffusion of gas molecules, in particular the smaller ones. A change in permeation due to change of stacking was also observed by Geim et al. in GO-epoxy laminates, where the interlayer spacing was tuned not by thermal annealing but by change in relative humidity[60]; also in this case, permeation rate was dependent on the ion diameter, and permeation increased with the increase of average stacking distance.

While changes in pH or humidity can allow a very effective tuning of permeability, they can be difficult or slow to achieve in an industrial environment. We believe that the thermal annealing approach described here could instead find a more straightforward application on large membranes as a post-fabrication enhancement of $(PDDA/GO)_{10}$ composites, and thus could be easily tuned and upscaled for application in gas separation technologies.

4. Experimental Section

Materials and Methods: Main reactants were purchased from the following companies: Sodium hydroxide (NaOH, ACS reagent grade) from Sigma–Aldrich, Ammonium fluoride (NH_4F, ACS reagent grade) from Aldrich, hydrofluoric acid 50 wt% (HF, A.C.S. reagent grade) from Carlo Erba Reagenti, chloroform ($CHCl_3$, A.C.S. reagent grade) from Merck. Deionized water (DI water) was produced by a Culligan deionizer, and neutralized by correcting its slightly acid pH with a 1 M NaOH water solution, controlling the pH with a pH-meter. A pH 8 + DHS was purchased from XS Instruments and equipped with a glass XS Polymer electrode. A 20 wt% water solution of PDDA was purchased by Aldrich, while a 0.4 wt% dispersion of GO was purchased by Graphenea. After proper dilution (final concentrations: PDDA 1% w/w, GO 0.01% w/w), PDDA was used without further operations while GO was sonicated for 4 h at 30–35 °C using a using a 10 L sonication bath commercialized by Elma (Elmasonic S100). Matrimid 5218 (Matrimid) yellow powder was kindly provided by Huntsman Corporation and used to prepare polymeric films without further purification. A 1.5 wt% Matrimid solution in dichloromethane (CH_2Cl_2, A.C.S. reagent grade, Merck) was used to prepare thin films (thickness ≈40 μm): 20 mL of Matrimid solution were placed in a glass petri dish (diameter = 9 cm).

After complete evaporation of the solvent (2 days), yellow thin films were in vacuum thermal treated at 200 °C for 18 h. Layer-by-layer self-assemblies were performed by a dedicated automated dip-coating apparatus following a previously reported procedure.[39] First, a Matrimid substrate was superficially hydrolysed with 18 h dipping in $NaOH_{(aq)}$, 1 M. A BiLayer (BL) was prepared by dipping fully treated Matrimid samples in a PDDA water solution (1% w/w) for 5 min. Excess of deposited polycation was removed by a 20 min rinse in neutralized water (pH = 7). Then, the sample was dipped in the GO water suspension (0.01 wt%) for 5 min and, once again, excess of deposited species was removed with a 20 min rinse in neutralized water. By repeating this procedure for ten times, a coating of 10BLs was prepared. At the end of the self-assembly, coated films were treated for 30 min under an IR lamp in order to remove residual water present in the coating, while keeping the superficial temperature below 54 °C. The multilayer samples prepared for SEM, XRD, and XPS analysis were fabricated using the same procedure but using as a substrate Matrimid spin-coated rectangular (1 cm x 2 cm) Si wavers (cut from commercial Boron-doped Si disc, Silicon Materials Inc.). All rectangular Si wafers were prior activated in NH_4F/HF water solution (10 min in six parts of 40% w/w NH_4F and one part of 50% w/w HF), extensively washed in deionized (DI) water and coated with a 5% w/w solution of Matrimid in 1,1,2,2 – Tetrachloroethane (ACS reagent grade, Merck) using an accelerated spin-coating procedure: 10 s at 500 rpm, 10 s at 1000 rpm, 10 s at 2000 rpm, 10 s at 3000 rpm, and 30 s at 4000 rpm. Spin-coating was repeated twice. Initial superficial hydrolysis was performed for just 5 min in $NaOH_{(aq)}$, 1 M. Water Contact Angles were determined using a drop shape analyzer (DSA30S-Kruss) depositing 4 μL of DI water drops. All ζ-potentials were recorded at pH = 7 in a $KCl_{(aq)}$, 1 mM with a SurPASS 3 (Anton Paar) equipped with an Adjustable Gap Cell (dimension: 10 mm x 20 mm). The morphology of the surface of the multilayers was analyzed by scanning electron microscopy (SEM), using a Field Emission Gun instrument (Tescan Mira3) equipped with energy dispersive spectrometry (EDS, Bruker probe). All SEM samples were made conductive by evaporation of gold before observation (Quorum Q150R ES + coater). Mechanical strain measurements were performed on the $(PDDA/GO)_{10}$ multilayers on matrimid, compared with the ones on bare matrimid substrates, but did not observe significant differences: Young modulus for bare matrimid was 3015 ± 329 MPa, it was 3150 ± 480 MPa for $(PDDA/GO)_{10}$. This could be expected, given that the matrimid polymer sheet is 40 μm thick, thus addition of ten layers of mechanically weak PDDA/GO (each layer being ≈1.4 Å, see XRD) will add only a very small improvement to the mechanical properties of the matrimid. All gas transport analyses were performed at 35 °C according to a manometric technique reported in ASTM D 1434.[61] All tested samples had an area of 2.2 cm^2 and applied Δp was in the range of 1.7–1.9 bar. XPS spectra were acquired by using hemispherical analyzer (Phoibos 100, Specs, Germany). Mg Kα excitation was used at 125 W(XR50, Specs, Germany). Survey and high-resolution spectra were acquired in Fixed Analyser Transmission (FAT) mode, with energy resolution 0.9 eV measured on freshly sputtered Silver (Ag 3d). Base pressure during the measurement was 10E-8 mbar. Spectrometer was calibrated to Au 4f7/2 peak at 84.0 eV. The silicon wafers were fixed on sample holder by conductive Carbon tape and degassed overnight. Charging effects were corrected by calibrating all spectra to C 1s 285 eV. Fit was performed by using CasaXPS software after Shirley background subtraction. C 1s was fitted according ref. Carbon 143, (2019) 268–275, by using asymmetric line-shape for aromatic Carbon and symmetric line-shapes (pseudo-voigt) for the C—O defects. The relative abundance of aromatic sp2 C=C was the main parameter obtained from C 1s fit, unfortunately the presence of different C—N groups overlaps the C—O groups. Si 2p was fitted by a doublet with fixed spin orbit split (0.63 eV). Survey spectra, binding energies, and relative atomic abundances were reported in SI for Silicon after HF/NH4F cleaning, Matrimid deposited on cleaned Silicon, $(PDDA/GO)_{10}$, and $(PDDA/GO)_{10}$ after annealing at different temperatures. Pristine GO and PDDA on Silicon were measured as references. XRD patterns were collected in specular geometry using the Smartlab Diffractometer equipped by a Cu-rotating anode ($\lambda = 1.54184$ Å) and a set of sollers and slits to reach a parallel beam with divergence 0.1° and acceptance 0.02°. The reported error associated with the interlayer spacing combines the experimental error and the peak fitting procedure.

The detector acceptance was 0.03°, which led to an error bar ranging from 0.04 to 0.07 Å for the Bragg peak positions varying from 8° to 6°. The values reported in the table came from the fitting procedure; they were more significant for high temperatures due to the lower signal-to-noise ratio. It used the fitting procedure implemented by Origin software, which use the Levenberg–Marquardt algorithm method.

Thermogravimetric and isothermogravimetric analyses (Perkin Elmer TGA4000) were used to evaluate thermal stability of neat GO and polyelectrolytes (PDDA, PSS) under a nitrogen atmosphere. For thermogravimetric analyses, samples were heated from 50 to 250 °C at 10 C min^{-1}. Neat GO was obtained from the concentrated commercial suspension after evaporation of the water, carried out in oven at 50 °C. Due to the tendency of solid GO to disperse out from the pan of the TGA upon heating, (iso)thermogravimetric analyses of graphenic powder were carried out using a thermal conductive paste (Thermigrease TG 20044). Briefly, the desired mass of GO (roughly 5 mg) was weighted into the TGA pan. Later, a proper amount of paste (roughly 60 mg) was exactly weighed into the same pan, and placed to fully cover the powder of GO. The (iso)thermogravimetric analyses were carried out up to a temperature of 250 °C (began of thermo degradation of the paste). In the final thermogram, the real masses of GO were calculated subtracting from the recorded mass the amount of paste located into the pan at the beginning of the analyses.

Statistical Analysis: All the permeances of the multilayers were calculated from the experimentally determined values of permeances according to equations presented in the Introduction. All data were presented as mean ± Standard Deviation and, in all cases, at least three independently prepared samples were tested.

Supporting Information

Supporting Information is available from the Wiley Online Library or from the author.

Conflict of Interest

The authors declare no conflict of interest.

Data Availability Statement

The data that support the findings of this study are available from the corresponding author upon reasonable request.

[1] A. N. Cobb, J. L. Thompson, *Environ. Model. Softw.* **2012**, *38*, 296.
[2] A. R. Davies, V. Castán Broto, S. Hügel, *Politics Gov.* **2021**, *9*, 1.
[3] P. Nema, S. Nema, P. Roy, *Renewable Sustainable Energy Rev.* **2012**, *16*, 2329.
[4] S. Solomon, G.-K. Plattner, R. Knutti, P. Friedlingstein, *Proc. Natl. Acad. Sci. USA* **2009**, *106*, 1704.
[5] A. Marra, E. Colantonio, *Socioecon Plann Sci* **2021**, *76*, 100958.
[6] 'A hydrogen strategy for a climate-neutral Europe', European Commission COM/2020/301 https://eur-lex.europa.eu/legal-content/EN/TXT/?uri=CELEX%3A52020DC0301 (accessed: October 2023).
[7] S. M. Ostojic, *Ann. Nutr. Metab.* **2019**, *75*, 195.
[8] V. Pierrard, *Planet. Space Sci.* **2003**, *51*, 319.
[9] T. Holm, T. Borsboom-Hanson, O. E. Herrera, W. Mérida, *Energy Convers. Manag.* **2021**, *237*, 114106.
[10] F. Dawood, M. Anda, G. M. Shafiullah, *Int. J. Hydrogen Energy* **2020**, *45*, 3847.
[11] I. K. Muritala, D. Guban, M. Roeb, C. Sattler, *Int. J. Hydrogen Energy* **2020**, *45*, 26022.
[12] S. M. Nazir, J. H. Cloete, S. Cloete, S. Amini, *Energy* **2019**, *185*, 372.
[13] R. S. Haszeldine, *Science* **2009**, *325*, 1647.
[14] Y. Le Moullec, T. Neveux, A. Al Azki, A. Chikukwa, K. A. Hoff, *Int. J. Greenh. Gas Control.* **2014**, *31*, 96.
[15] A. B. Hinchliffe, K. E. Porter, *Chem. Eng. Res. Des.* **2000**, *78*, 255.
[16] D. W. Breck, *Zeolite Molecula Sieves: Structure, Chemistry, and Use*, Wiley, Hoboken, NJ **1973**.
[17] L. Shao, B. T. Low, T. S. Chung, A. R. Greenberg, *Vol.* **2009**, *327*, 18.
[18] J. G. Wijmans, R. W. Baker, *J. Membr. Sci.* **1995**, *107*, 1.
[19] M. Karunakaran, L. F. Villalobos, M. Kumar, R. Shevate, F. H. Akhtar, K.-V. Peinemann, *J. Mater. Chem. A* **2017**, *5*, 649.
[20] R. Abedini, A. Nezhadmoghadam, *Petroleum & Coil* **2010**, *52*, 69.
[21] L. M. Robeson, *J. Membr. Sci.* **2008**, *320*, 390.
[22] S.-K. Ryi, C.-B. Lee, S.-W. Lee, J.-S. Park, *Energy* **2013**, *51*, 237.
[23] C. A. Scholes, K. H. Smith, S. E. Kentish, G. W. Stevens, *Int. J. Greenh. Gas Control.* **2010**, *4*, 739.
[24] S. P. Cardoso, I. S. Azenha, Z. Lin, I. Portugal, A. E. Rodrigues, C. M. Silva, *Sep. Purif. Rev.* **2018**, *47*, 229.
[25] S. Matteucci, Y. Yampolskii, B. D. Freeman, I. Pinnau, in *Materials Science of Membranes for Gas and Vapor Separation* (Eds.: Y. Yuri, P. Ingo, F. Benny), Wiley, Hoboken, NJ **2006**, 1.
[26] L. Dong, M. Chen, J. Li, D. Shi, W. Dong, X. Li, Y. Bai, *J. Membr. Sci.* **2016**, *520*, 801.
[27] D. Bouša, K. Friess, K. Pilnáček, O. Vopička, M. Lanč, K. Fónod, M. Pumera, D. Sedmidubský, J. Luxa, Z. Sofer, *Chem. - Eur. J.* **2017**, *23*, 11416.
[28] H. W. Kim, H. W. Yoon, S.-M. Yoon, B. M. Yoo, B. K. Ahn, Y. H. Cho, H. J. Shin, H. Yang, U. Paik, S. Kwon, J.-Y. Choi, H. B. Park, *Science* **2013**, *342*, 91.
[29] K. Guan, J. Shen, G. Liu, J. Zhao, H. Zhou, W. Jin, *Sep. Purif. Technol.* **2017**, *174*, 126.
[30] R. Zeynali, K. Ghasemzadeh, A. B. Sarand, F. Kheiri, A. Basile, *Catal. Today* **2019**, *330*, 16.
[31] A. Achari, M. Eswaramoorthy, *J. Phys. Condens. Matter.* **2016**, *4*, 7560.
[32] C. Y. Chuah, L. Nie, J. M. Lee, T. H. Bae, *Sep. Purif. Technol.* **2020**, *246*, 116933.
[33] R. Zeynali, K. Ghasemzadeh, A. B. Sarand, F. Kheiri, A. Basile, *Sep. Purif. Technol.* **2018**, *200*, 169.
[34] V. Palermo, *Chem. Commun.* **2013**, *49*, 2848.
[35] D. R. Dreyer, S. Park, C. W. Bielawski, R. S. Ruoff, *Chem. Soc. Rev.* **2010**, *39*, 228.
[36] Z. Y. Xia, D. Wei, E. Anitowska, V. Bellani, L. Ortolani, V. Morandi, M. Gazzano, A. Zanelli, S. Borini, V. Palermo, *Carbon N Y* **2015**, *84*, 254.
[37] J. S. Sanchez, J. Xu, Z. Xia, J. Sun, L. E. Asp, V. Palermo, *Compos. Sci. Technol.* **2021**, *208*, 108768.

[38] Z. Y. Xia, M. Christian, C. Arbizzani, V. Morandi, M. Gazzano, V. Quintano, A. Kovtun, V. Palermo, *Nanoscale* **2019**, *11*, 5265.

[39] D. Pierleoni, M. Minelli, S. Ligi, M. Christian, S. Funke, N. Reineking, V. Morandi, F. Doghieri, V. Palermo, *ACS Appl. Mater. Interfaces* **2018**, *10*, 11242.

[40] D. Gero, *Science* **1997**, *277*, 1232.

[41] E. Treossi, M. Melucci, A. Liscio, M. Gazzano, P. Samorì, V. Palermo, *J. Am. Chem. Soc.* **2009**, *131*, 15576.

[42] S. P. Koenig, L. Wang, J. Pellegrino, J. S. Bunch, *Nat. Nanotechnol.* **2012**, *7*, 728.

[43] S. Zhao, H. Zhu, H. Wang, P. Rassu, Z. Wang, P. Song, D. Rao, *J. Hazard. Mater.* **2019**, *366*, 659.

[44] G. Dong, J. Hou, J. Wang, Y. Zhang, V. Chen, J. Liu, *J. Membr. Sci.* **2016**, *520*, 860.

[45] X. Shan, Y. Lin, A. Zhao, Y. Di, Y. Hu, Y. Guo, Z. Gan, *Nanotechnology* **2019**, *30*, 425403.

[46] C.-Z. Liang, S.-P. Sun, F.-Y. Li, Y.-K. Ong, T.-S. Chung, *J. Membr. Sci.* **2014**, *469*, 306.

[47] M.-J. Li, C.-M. Liu, Y.-B. Xie, H.-B. Cao, H. Zhao, Y. Zhang, *Carbon N Y* **2014**, *66*, 302.

[48] W. Wei, S. Yang, H. Zhou, I. Lieberwirth, X. Feng, K. Müllen, *Adv. Mater.* **2013**, *25*, 2909.

[49] J. Lee, J. H. Jang, H.-R. Chae, S. H. Lee, C.-H. Lee, P.-K. Park, Y.-J. Won, I.-C. Kim, *J. Mater. Chem. A.* **2015**, *3*, 22053.

[50] A. Kovtun, D. Jones, S. Dell'elce, E. Treossi, A. Liscio, V. Palermo, *Carbon N Y* **2019**, *143*, 268.

[51] X. Liu, J. E. Whitten, *Thin Solid Films* **2003**, *434*, 145.

[52] A. Kovtun, A. Candini, A. Vianelli, A. Boschi, S. Dell'elce, M. Gobbi, K. H. Kim, S. Lara Avila, P. Samorì, M. Affronte, A. Liscio, V. Palermo, *ACS Nano* **2021**, *15*, 2654.

[53] F. Perrozzi, S. Prezioso, L. Ottaviano, *J. Phys.: Condens. Matter* **2015**, *27*, 013002.

[54] K. Erickson, R. Erni, Z. Lee, N. Alem, W. Gannett, A. Zettl, *Adv. Mater.* **2010**, *22*, 4467.

[55] S. Khaliha, T. D. Marforio, A. Kovtun, S. Mantovani, A. Bianchi, M. L. Navacchia, M. Zambianchi, L. Bocchi, N. Boulanger, A. Iakunkov, M. Calvaresi, A. v. Talyzin, V. Palermo, M. Melucci, *FlatChem* **2021**, *29*, 100283.

[56] X. Díez-Betriu, F. J. Mompeán, C. Munuera, J. Rubio-Zuazo, R. Menéndez, G. R. Castro, A. De Andrés, *Carbon N Y* **2014**, *80*, 40.

[57] J. Sun, F. Morales-Lara, A. Klechikov, A. V. Talyzin, I. A. Baburin, G. Seifert, F. Cardano, M. Baldrighi, M. Frasconi, S. Giordani, *Carbon N Y* **2017**, *120*, 145.

[58] J. Sun, M. Sadd, P. Edenborg, H. Grönbeck, P. H. Thiesen, Z. Xia, V. Quintano, R. Qiu, A. Matic, V. Palermo, *Sci. Adv.* **2021**, *7*, 812.

[59] D. V. Andreeva, M. Trushin, A. Nikitina, M. C. F. Costa, P. V. Cherepanov, M. Holwill, S. Chen, K. Yang, S. W. Chee, U. Mirsaidov, A. H. Castro Neto, K. S. Novoselov, *Nat. Nanotechnol.* **2021**, *16*, 174.

[60] J. Abraham, K. S. Vasu, C. D. Williams, K. Gopinadhan, Y. Su, C. T. Cherian, J. Dix, E. Prestat, S. J. Haigh, I. V. Grigorieva, P. Carbone, A. K. Geim, R. R. Nair, *Nat. Nanotechnol.* **2017**, *12*, 546.

[61] ASTM D 1434 –82 (Reapproved 2015), Standard Test Method for Determining Gas Permeability Characteristics of Plastic Film and Sheeting.